

# Synthesis and Characterisation of Platinum Nanoparticles Capped with Isolated Zinc Species in SBA-15 channels: the Wall Effect

Elizabeth Raine<sup>a†</sup>, Adam H. Clark<sup>b†</sup>, Glen Smales<sup>b</sup>, Andrew Smith<sup>c</sup>, Diego Gianolio<sup>c</sup>, Tong Li<sup>d</sup>, Jianwei Zheng<sup>a</sup>, Benjamin E. Griffith<sup>e</sup>, Tim I. Hyde<sup>f</sup>, Mark Feaviour<sup>f</sup>, Paul Collier<sup>f</sup>, John V. Hanna<sup>e</sup>, Gopinathan Sankar<sup>b</sup> and Shik Chi Edman Tsang<sup>a\*</sup>.

a. Wolfson Catalysis Centre, Department of Chemistry, University of Oxford, Oxford, OX1 3QR, UK.

b. Department of Chemistry, University College London, 20 Gordon Street, WC1E 0AJ, London, UK.

c. Diamond Light Source Ltd, Harwell Science and Innovation Campus, Didcot, Oxfordshire, OX11 0DE, UK

d. Institute for Materials & ZGH, Ruhr-Universität Bochum, Universitätsstr. 150, 44801 Bochum, Germany

e. Department of Physics, University of Warwick, Coventry, CV4 7AL, United Kingdom

f. Johnson Matthey, Blount's Court, Sonning Common, Reading, RG4 9NH, UK

† First author with equal contribution.

*KEYWORDS (Word Style "BG\_Keywords").*

---

**ABSTRACT:** The strong directing effects and difficulties in the removal of organic based surfactants makes the templated synthesis of nanoparticles in solid porous structures of defined molecular sizes such as SBA-15, without the use of surfactants, considerable attractive. However, the effects of their internal surface structures, adsorption affinities and lattice mismatch on the particle morphology grown therein have not been fully appreciated. Here, we report the internal surface of the silica preferentially hosts isolated tetrahedrally coordinated oxidic Zn species on the molecular walls of the SBA-15 channels from wet impregnated Zn<sup>2+</sup> and Pt<sup>2+</sup> species. This leads to less thermodynamic stable but kinetic controlled configuration of atomic zinc deposition on core platinum nanoparticles with unique confined lattice changes and surface properties to both host and guest structures at the interface upon reduction of the composite. This method on templated nanoparticles may generate interests to form new catalytic tunable materials.

---

With increasing world population<sup>1</sup>, diminishing access to fossil fuel reserves<sup>2</sup> and a rapidly developing world, the need for new or more efficient routes of energy and chemicals provisions has never been more vital.<sup>3</sup> Tailoring catalyst structures and surfaces for specific chemical reactions to improve catalytic efficiencies is continuously of interest to the catalysis community. Many bimetallic catalysts have recently been found to show superior activity or selectivity than their monometallic counterparts due to surface site blocking and electronic modulation.<sup>4,5</sup> For example, bimetallic nanoparticles containing platinum are often used in catalytic reactions with low activation barriers and enhanced activity or selectivity.<sup>6</sup> Platinum zinc species are reported to be active for hydrogenation and dehydrogenation reactions.<sup>7–9</sup>

However, size control in bimetallic nanoparticles is commonly achieved in the presence of surfactants or polymers which may impair working catalysts and are not easy to remove for most catalytic applications.<sup>10</sup> There are some recently reported surfactant-free syntheses methods in catalyst preparation.<sup>11–14</sup> Synthesis of these bimetallic nanoparticles inside thermally stable porous structures as supports, without separating the templates,

perhaps represents one of the most attractive methods.<sup>15,16</sup>

Supported nanoparticles have been well researched along with the introduction of the smallest particle possible, single-atom catalysts.<sup>17–19</sup> Surface decoration by single atoms on monometallic particles are anticipated to give high catalytic performances.<sup>20–22</sup> For example, it has been seen that zinc deposited on a copper nanoparticle has increased catalytic ability with enhanced formate binding.<sup>23</sup>

One method of synthesizing single isolated sites is through the use of ion-exchange Bronsted proton of Al sites in zeolites. It has been seen that Zn<sup>2+</sup> species can be exchanged with the protonic sites in the zeolite surface leaving isolated Zn ions immobilised in the zeolite walls.<sup>24,25</sup> The introduction of these dopant ions into the zeolite walls can lead to the formation Lewis acid sites.<sup>24,26</sup> The nature of these acidic sites can depend on the synthesis method, as well as the dopant type and concentration. Various methods of binding Zn<sup>2+</sup> onto the surfaces of zeolites and silicas have been discussed, many proposing a tetrahedral coordinated species with the surface oxygens binding to the Zn<sup>2+</sup>, allowing it to be capped

by other reagents.<sup>25,27</sup> These zinc modified zeolites have been shown to have enhanced catalytic behaviour for methane activation as well as propylene hydrogenation.<sup>28,29</sup> Further investigation was performed on zincosilicate CIT-6 leading to enhanced Diels-Alder reactivity which was not previously possible with alternative dopants.<sup>30</sup> However, the small size of internal cavities of zeolites do not allow the synthesis of metal nanoparticles to be decorated with these isolated species.

There has been a previous attempt utilising the mesoporous channels of SBA-15 silica as a porous support to promote a core-shell growth of AgNi particles<sup>31</sup> without the use of a surfactant. The 1-dimensional channels not only restrict the particle growth ensuring a small particle size distribution, but are thought to encourage the two metal precursors to grow separately forming a phase boundary under mild reduction temperatures as benign hosts. The core and shell thickness can be tuned by using different precursor ratios. The incorporation of Ni to Ag particles of defined particle size may generate new catalysts for selective hydrogenation.<sup>32–34</sup> It is, however, the effects of the internal surface structure of SBA-15, surface affinities and lattice mismatches on the metallic particle morphology grown therein and vice versa to the SBA-15 host structure have not been fully appreciated.

Here, we report the synthesis of the PtZn bimetallic system in SBA-15 channels using the same methodology. Instead of obtaining thermodynamic more stable Pt-Zn core-shell or their homogeneous alloy structure, it is interesting to see the surface atomic doping of Zn atoms on the core Pt nanoparticles with kinetic controlled lattices at the materials interface, in this porous template after mild reduction. We attribute this interesting observation to the high affinity of silica walls as the main influencing factor for hosting  $Zn^{2+}$ , allowing preferential homogeneous wetting on silica internal surface during preparation, presumably due to comparable bonding environment and hydrophilic properties. In addition, the structural mismatches of host and guest can also affect their final lattice parameters, giving the fundamental basis for new catalytic properties of the composites. Thus, we also show that the effects on the porous template structure in molecular dimensions, internal surface structure and chemical affinity play important roles to the growth of nanoparticles therein and could not be ignored. It is anticipated that the rationalizations may be further developed as a new synthesis method for atomic deposition of metal nanoparticles within porous template structures.

## Results and discussion

Platinum zinc of differing compositions ( $Pt_2Zn_8$ ,  $Pt_5Zn_5$ ,  $Pt_8Zn_2$ ) along with monometallic Pt and Zn were synthesized without the use of surfactants within the 1-dimensional channels of the mesoporous silica support, SBA-15, in order to encourage small nanoparticle growth therein. These bimetallic PtZn/SBA-15 particles after reduction, along with the Zn/SBA-15 and Pt/SBA-15 monometallic comparison samples, are extensively characterized by Transmission Electron Microscopy (TEM), Low Energy Ion Scattering (LEIS), X-Ray Absorption Spectroscopy (XAS), Wide Angle X-ray Scattering (WAXS), Small Angle X-ray Scattering (SAXS) and

Atom Probe Tomography (APT) for a full structural and spatial understanding.

Transmission Electron Microscopy (TEM) images were taken of the samples prepared through the reported synthesis in order to confirm the nanoparticle formation inside the silica channels and ensure no larger particles were aggregating on the silica surface. To control the particle size and distribution of the two metals, the particles must form inside the channels rather than on the external silica surface. Figure 1A, which shows the particles are well distributed inside the SBA-15 channels and with no larger aggregated particles on the outside of the porous silica. This was confirmed by secondary electron imaging, Figure 1C, showing that there are no particles on the surface of the silica in the same region where particles are seen in the bright field image, Figure 1B. The  $Pt_2Zn_8$ /SBA-15 nanoparticles have a mean diameter of 4.2 nm ( $\pm 1.9$  nm), which is narrower than the average SBA-15 channel diameter of 6.5 nm (S1) meaning that the channels are not blocked for any reactants. This is also valid for the  $Pt_5Zn_5$ /SBA-15 and the  $Pt_8Zn_2$ /SBA-15 which have mean diameters of 3.2 nm ( $\pm 2.3$  nm) and 3.1 nm ( $\pm 1.5$  nm) respectively (S2&S3). Pt/SBA-15 nanoparticles show a similar particle size of 3.1 nm ( $\pm 1.5$  nm) (S4). Interestingly, in the direct comparison with Pt nanoparticles, no particles or areas of material aggregation could be seen in the Zn/SBA-15 sample, indicating much smaller Zn species were present (Figure 2), indicative of the strong wetting properties of silica walls towards Zn species.

Scanning EDX was performed in conjunction with the secondary electron imaging in order to understand the elemental distribution of these samples. Figure 1 D, E & F shows the presence of both platinum and zinc in the nanoparticles, with zinc located fully across the silica support, indicating the zinc spreads across the walls of the silica rather than being only deposited at the platinum particles. The higher density regions of zinc near the platinum suggest that there is a favourable interaction between the zinc and the platinum with platinum particles capped with zinc species on the silica surface (see further TEM and EDX in SI S1-S5).

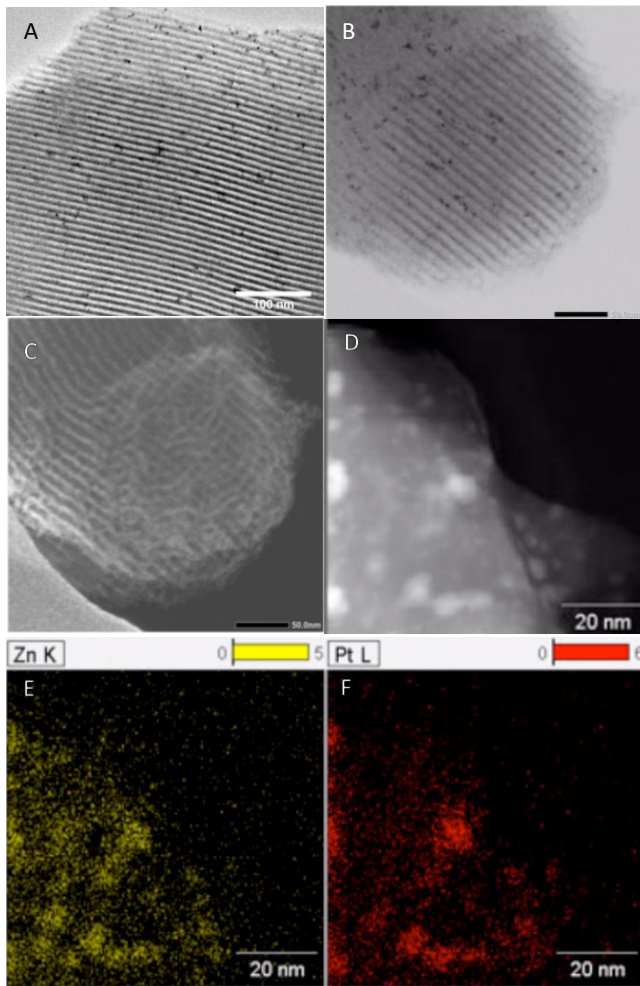


**Figure 1.** A) TEM image of Pt<sub>2</sub>Zn<sub>8</sub>/SBA-15. B) Bright field image of Pt<sub>2</sub>Zn<sub>8</sub>/SBA-15. C) Corresponding secondary electron image. D) Scanning EDX data from Pt<sub>2</sub>Zn<sub>8</sub>/SBA-15 sample with E) EDX map of Zn distribution and F) EDX map of Pt distribution.

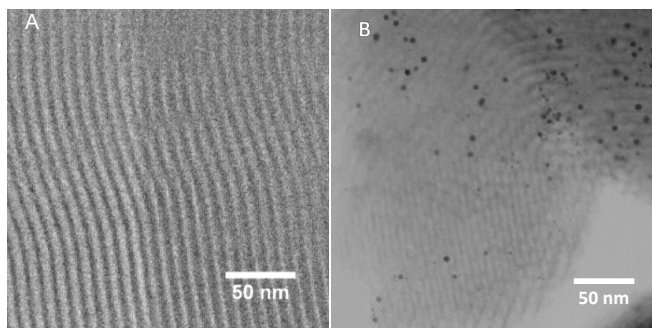


**Figure 2.** TEM image at 40K magnification of A) Zn/SBA-15 and B) Pt/SBA-15

Low Energy Ion Scattering (LEIS) was used to identify the elemental composition of Pt<sub>2</sub>Zn<sub>8</sub>/SBA-15 sample at various particle depths by stripping its surface with high energetic Ne<sup>+</sup>. Figure 3A shows that the first scan of 0.06

nm correlating to the surface of the silica channels where mainly Zn is present, with only a very small Pt quantity. There is a dramatic increase in Pt intensity as the depth increases to 3.9nm. According to our peaks fitted with average spherical particles, it is clear that the Pt intensity is much increased on probing deeper into the particle, Figure 3B. Thus, the high zinc content in the first scan indicates that there is zinc enrichment at the surface of the SBA-15 channels. After removal of the silica surface and zinc, the platinum becomes more prominent, the zinc signal remains intense due to the zinc across the surface of the SBA-15 channel. This result is consistent with the EDX result, showing the surprisingly enrichment of zinc content on the silica walls.

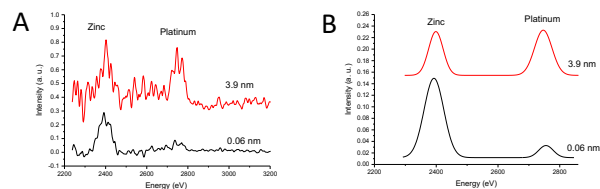


**Figure 3.** Low Energy Ion Scattering spectrum from Pt<sub>2</sub>Zn<sub>8</sub>/SBA-15 showing Zn on the particle surface (black) and Pt and Zn at lower depths (red). A) Plot showing Pt content increase with increasing depth into the sample. B) Peak fitting of the surface analysis (black) and the 3.9 nm depth (red) indicating the greater Pt presence deeper into the particles.

X-ray Absorption Spectroscopy (XAS) on the Zn K-edge was used to further investigate the structure of the zinc in the silica walls. The Zn K-edge XANES shows a different profile to many standard zinc salts tested as shown in Figure 4A indicating that the formation of a common salt is not occurring. Indeed, the best agreement of the Zn/SBA-15 experimental spectra is with modelled isolated zinc tetrahedra from FDMNES35,36 modelling calculations, as shown in Figure 4C. This suggests that the zinc is bonded to the silica walls forming isolated tetrahedrally coordinated oxidic species. Instead of getting the extended tetrahedral sharing units of ZnO, Zn(OH)<sub>2</sub> or related bulk solid structures, these Zn-O tetrahedra are clearly isolated zinc species as shown by the absence of long-range order in the EXAFS region with no Zn-Zn interactions (S8). Figure 4B shows that on increasing the zinc content in the Pt-Zn/SBA-15 series, the white line intensity decreases and the peak splits into a strong doublet which agrees with the results which have been previously reported by Mei et al. who attributed the formation of [ZnO<sub>4</sub>]<sup>6-</sup> on silica surfaces.<sup>37</sup> The similarity in lattice and coordination number matching with internal silica surface appears to offer a strong directing role to bind Zn ions preferentially from the mixture of Pt and Zn precursors.

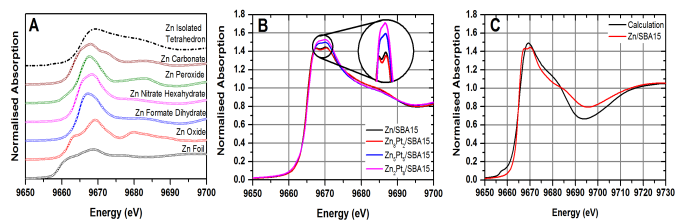


**Figure 4.** A) A comparison of measured Zn standard materials and the Zn isolated tetrahedron result of the FDMNES calculation. B) Zn K-edge XANES plot of the Zn/SBA-15 and PtZn/SBA-15 series from B18 at Diamond Light Source. C) A direct comparison of the experimental Zn/SBA-15 Zn K-edge XANES spectrum measured and the FDMNES calculated spectra for Zn isolated tetrahedron.

Analysis of the Zn K edge EXAFS demonstrates there is no long range ordered structure present in the local coordination environment of the Zn atoms. Fitting to the EXAFS has been performed using the Demeter software package. The amplitude reduction factor was determined by fitting to a ZnO standard material. The Fourier Transform range used was  $2.4 - 9.7 \text{ \AA}^{-1}$  and the fitting was performed in R space. A Zn-O scattering path was fitted with all parameters free with the results shown in Table 1 below. Example fitting to the Zn/SBA15 sample are shown in figure 5, remaining figures for all samples are shown in the supplementary information. The fitting results demonstrate that in all samples Zn is found to be present in isolated oxidic tetrahedral with no ordered extended local structure suggesting a disordered binding to the silica wall.

**Table 1** of results for EXAFS fitting performed on the Zn K edge

| Sample                          | R( $\text{\AA}$ ) | $\sigma^2$ | N   |
|---------------------------------|-------------------|------------|-----|
| Zn                              | 1.97              | 0.00752    | 4.0 |
| Zn <sub>8</sub> Pt <sub>2</sub> | 1.96              | 0.00778    | 4.0 |
| Zn <sub>5</sub> Pt <sub>5</sub> | 1.97              | 0.00880    | 3.9 |
| Zn <sub>2</sub> Pt <sub>8</sub> | 1.98              | 0.00921    | 3.9 |

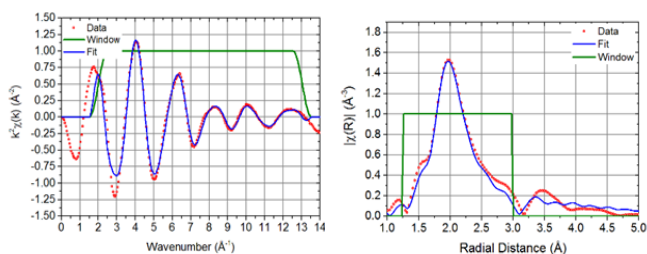


**Figure 5.** Zn K-edge EXAFS fitting example for the Zn/SBA-15 sample demonstrating the fit to K-space and for R-space in left and right respectively.

The platinum structure and electronic properties were also investigated with XAS on the Pt L<sub>3</sub> -edge. The XANES shows that there is a combination of both the metallic and a small amount of oxidic phase in the platinum particles in the structure after reduction, Figure 6. The pure Pt/SBA-15 sample shows the most metallic

nature with a higher oxide component when zinc is introduced into the system, although this oxidic nature does not continue to increase on increasing the zinc content. The exact fraction of the oxidic component in the PtZn/SBA-15 samples is not yet known as the particle size effects of metal clusters on the XANES spectrum make the linear combination fitting not possible<sup>38-41</sup>.

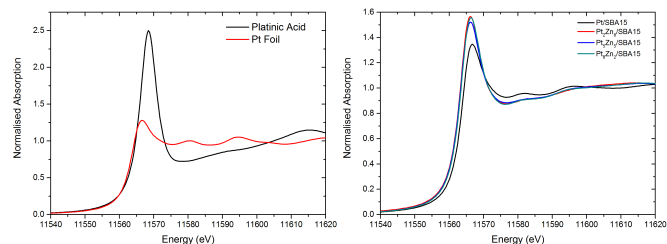


**Figure 6.** A) Pt L<sub>3</sub>-edge XANES comparison of the standard Pt materials, platonic acid and metallic Pt, with B) the Pt/SBA-15 and three PtZn/SBA-15 materials.

Analysis of the Pt L<sub>3</sub> edge EXAFS has been performed to determine the average local structure around the absorbing Pt atoms, the results are shown in Table 2. Fitting was performed using a Fourier transform range of  $K 2.8 - 10.8 \text{ \AA}^{-1}$  allowing for refinement of Pt-Pt and Pt-O coordination shells associated to oxide and metallic components. The amplitude reduction factor was determined through fitting performed over the aforementioned K range to a Pt metal foil reference data using the Demeter software package. During refinement the Pt-O bond distance and  $\sigma^2$  parameters were held fixed from an initial refinement performed on the Pt<sub>2</sub>Zn<sub>8</sub>/SBA-15 (most oxidic) sample due to high correlation with the coordination number. The  $\sigma^2$  parameter for the Pt-Pt coordination shell was refined from the Pt/SBA-15 sample (most metallic) and held constant for the remaining samples. From this analysis a clear trend can be observed, with decreasing Pt content there is a decreasing proportion of Pt than is found in metallic state. Example fitting is shown in figure 6 for the Pt<sub>8</sub>Zn<sub>2</sub>/SBA-15 sample, remaining samples are shown in supplementary figures. From these results it is proposed that the Pt exists as a metallic nanoparticle with a oxide surface shell. By assuming a spherical nanoparticle model it is possible to obtain an estimate for the metallic Pt core diameter: 2.6 nm, 1.4 nm, 1.5nm and 1.2 nm respectively in order of highest Pt content.

**Table 2** Table of results for EXAFS fitting performed on the Pt L3 edge

| Sample                          | Pt-O              |            |     | Pt-Pt             |            |     |
|---------------------------------|-------------------|------------|-----|-------------------|------------|-----|
|                                 | R( $\text{\AA}$ ) | $\sigma^2$ | N   | R( $\text{\AA}$ ) | $\sigma^2$ | N   |
| Pt                              | 2.00              | 0.00859    | 1.4 | 2.75              | 0.00734    | 4.2 |
| Pt <sub>8</sub> Zn <sub>2</sub> | 2.00              | 0.00859    | 2.6 | 2.74              | 0.00734    | 2.6 |
| Pt <sub>5</sub> Zn <sub>5</sub> | 2.00              | 0.00859    | 2.4 | 2.73              | 0.00734    | 2.8 |
| Pt <sub>2</sub> Zn <sub>8</sub> | 2.00              | 0.00859    | 2.7 | 2.71              | 0.00734    | 2.1 |

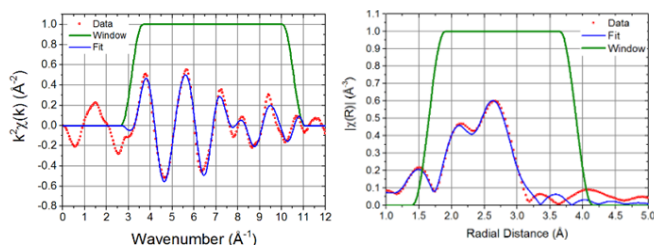


**Figure 7.** Pt L<sub>3</sub>-edge EXAFS fitting example for the Pt<sub>3</sub>Zn<sub>2</sub>/SBA-15 sample demonstrating the fit to K-space and for R-space in left and right respectively.

Wide Angle X-ray Scattering (WAXS) was used to analyse the crystalline structural component in the samples. It can be seen in Figure 8 that each platinum containing sample has reflection peaks which correspond well to the known metallic platinum crystal structure of 3.924(2) Å (red) but with slight smaller lattice parameter of 3.890(1) Å. This confirms the extended crystalline metallic structural phase of the Pt/SBA-15 but the slight small lattice is thought to be due to the distortion of Pt on the porous silica template internal surface. In contrast to XAS, no oxidic platinum phase is observed by this technique which indicates that this phase is particularly small or non-crystalline. Additionally, there are no crystalline peaks in the Zn/SBA-15 sample, confirming the high dispersion of the isolated zinc species likely in the silica walls rather than the presence of oxidic Zn or Zn containing particles. The gradual decrease in peak intensity down the patterns is indicative of the decreasing Pt content in the samples leading to decreased crystallinity and particle size. As the Pt content decreases, there is also a small but progressive shift to higher Q space, indicating a further contraction of lattice parameter. This shift correlates to a face centred cubic lattice parameter decrease from 3.890(1) Å for Pt/SBA-15 to 3.830(1) Å for Pt<sub>2</sub>Zn<sub>8</sub>/SBA-15. Thus, we attribute the main change in lattice parameter to the inclusion of zinc decoration on the Pt nanoparticles.

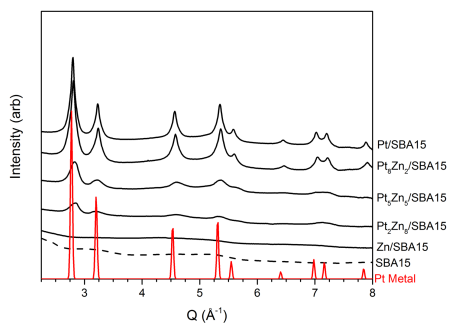


**Figure 8.** Stacked figure showing the WAXS obtained on each sample with a metallic Pt phase shown in red below for comparison illustrating the Bragg diffraction peaks are synonymous to metallic Pt or PtZn particles within the SBA-15 channels.

Small Angle X-ray Scattering (SAXS) was also used to investigate the changes in SBA-15 support lattice in re-

vers manner upon the introduction of the metals. Figure 9a shows the Bragg reflections from the stacking of the SBA-15 in each sample. All samples show the same hexagonal structure as the bare support (black), however there is seen to be some peak splitting in the samples containing the Pt particles. This is due to a change in lattice parameter in some of the SBA-15 after introduction of the metal particles. Fitting of the (200) reflection was accomplished using a two-peak fitting model with the resultant lattice parameters being derived by consideration of the Bragg scattering from a hexagonal lattice structure with an infinite pores along the c axis, example fitting is shown in Figure 9b. The fraction of distorted SBA-15 is given in Table 3 where the maximum distortions are observed for Pt<sub>5</sub>Zn<sub>5</sub>/SBA-15 and Pt<sub>2</sub>Zn<sub>8</sub>/SBA-15 with the alteration in lattice parameter ( $a_2$ ) fraction of approximately 31-32%.

**Table 3.** Extracted hexagonal lattice parameters for the SBA-15 structure derived from the Bragg reflections within the SAXS.

| Sample                                  | $a_1$ (Å) | Fraction | $a_2$ (Å) | Fraction |
|---|-----------|----------|-----------|----------|
| SBA-15                                  | 112.81(1) | 0.98(4)  | 109.60(6) | 0.02(4)  |
| Pt/SBA-15                               | 113.21(1) | 0.80(7)  | 110.08(3) | 0.20(7)  |
| Pt <sub>3</sub> Zn <sub>2</sub> /SBA-15 | 112.88(1) | 0.75(6)  | 110.55(2) | 0.25(6)  |
| Pt <sub>5</sub> Zn <sub>5</sub> /SBA-15 | 113.06(1) | 0.68(8)  | 110.05(2) | 0.32(8)  |
| Pt <sub>2</sub> Zn <sub>8</sub> /SBA-15 | 112.73(1) | 0.89(8)  | 109.96(9) | 0.31(8)  |
| Zn/SBA-15                               | 112.86(1) | 0.85(8)  | 109.88(6) | 0.15(8)  |

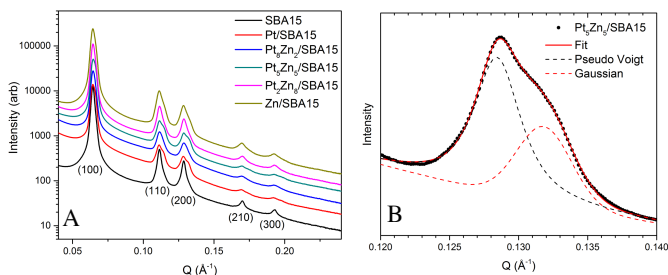


**Figure 9.** A) stacked plot displaying the indexed Bragg reflections from the hexagonal SBA-15 lattice observed using SAXS. B) Two-peak fitting to the (200) Bragg reflection for the Pt<sub>5</sub>Zn<sub>5</sub>/SBA-15 sample showing clear peak splitting.

McSAS fitting has been employed to analyse the particle size distribution within the SBA-15 samples<sup>42</sup> Here the Bragg reflections have been removed from fitting. Figure 10 gives the size distribution present exhibiting two clear features. The first relating to the Pt particles within the SBA-15 pores and the second to the SBA-15 pores. There is no result given for the Zn/SBA-15 sample as this failed to converge and no clear crystalline particles due to Zn are expected to be observed.

Table 4 gives the average Pt particle diameter and average SBA-15 pore diameter results. Here there is an ob-

served trend in the Pt particle size dependant on the atom fraction of Pt within each sample, with larger particles observed with increased Pt content. It is interesting to note that the pore diameter of SBA-15 is also greatly distorted from 6.0 nm to 5.4nm in the Pt<sub>5</sub>Zn<sub>5</sub>/SBA-15 and Pt<sub>2</sub>Zn<sub>8</sub>/SBA-15 samples, presumably due to the presence of the large crystalline Pt and the amorphous Zn coating.

**Table 4. Average particle and pore size diameters (wall thickness inclusive) derived from McSAS fitting of the SAXS form factor. Here the error is associated to the spread of sizes observed to 1 standard deviation.**

| Sample                                  | Pt Diameter (nm) | Pore Diameter (nm) |
|---|------------------|--------------------|
| Pt/SBA-15                               | 3.7 ± 1.7        | 6.0 ± 2.5          |
| Pt <sub>8</sub> Zn <sub>2</sub> /SBA-15 | 3.6 ± 1.7        | 6.1 ± 2.5          |
| Pt <sub>5</sub> Zn <sub>5</sub> /SBA-15 | 3.3 ± 1.6        | 5.5 ± 2.8          |
| Pt <sub>2</sub> Zn <sub>8</sub> /SBA-15 | 3.3 ± 1.6        | 5.4 ± 2.8          |

In restricted geometries, substrate molecules can interact with internal wall surfaces strongly through hydrophobic and hydrophilic interactions with or without hydrogen-bond interactions. This may lead to high activity and selectivity towards catalytic reactions of particular substrate molecules. It is noted that the partial ordering of the water molecules has been reported in the vicinity of the confining surfaces, such as in zeolites or cements, or water molecules in hydration shells of proteins.<sup>43</sup> Specifically, the existence of different kinds of water in pores, free water in the center of the pore and bound water near the pore surface, has been previously established by a variety of experimental techniques.<sup>43</sup> Analyzing these structures may help in the understanding of the hydrophilic or hydrophobic-surface interaction at the molecular level.

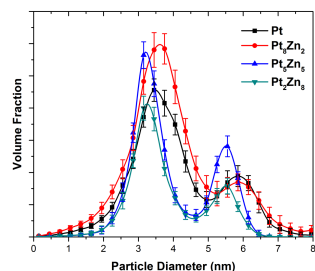


**Figure 10. Particle size distributions within the SBA-15 samples showing a doublet relating to the Pt particles at approximately 3 nm and the larger pore size of approximately 5.5 nm extracted using McSAS.**

The solid state <sup>29</sup>Si, <sup>1</sup>H and <sup>195</sup>Pt NMR data measured from the suite of samples is exhibited in Figure 11 and reported in Table 5. All deconvoluted and simulated <sup>29</sup>Si MAS NMR data shown in Figure 10a and Figure S7a clearly indicate that the Q<sup>n</sup> Si speciation defining the SBA-15 silicate network is described by Si(OSi)<sub>n</sub>O(R)<sub>4-n</sub>

(with R = Zn or H) and is represented by Q<sup>2</sup>, Q<sup>3</sup> and Q<sup>4</sup> species with the corresponding <sup>29</sup>Si resonances observed at δ ~91, ~102 and ~110 ppm, respectively. As expected for the mesoporous SBA-15 sample, the network is dominated by Q<sup>4</sup> units comprising ~84 % of the total Si speciation, with Q<sup>3</sup> (~12 %) and Q<sup>2</sup> (~4 %) species constituting minor components. A useful parameter elucidated from the quantitative <sup>29</sup>Si MAS NMR data used to describe network alteration upon the incorporation of network forming and/or network modifying cations is the network connectivity (NC) defined by: NC = (Q<sup>1</sup>% + 2Q<sup>2</sup>% + 3Q<sup>3</sup>% + 4Q<sup>4</sup>%) / 4.44–47

Previous studies of Zn incorporation into biomaterial and glass formulations have demonstrated that Zn exhibits both network forming and network modifying characteristics; 48–50 elements of this behaviour able to be identified upon Zn incorporation into the SBA-15 network.

From the incorporation of Zn to form the Zn/SBA-15 sample, it can be observed from the <sup>29</sup>Si MAS NMR data of Figure 10a and integrated intensities in Table 3 that the relative populations of the Q<sup>3</sup> species increases by ~18% and NC drops from 3.81 to 3.62 in comparison to the native SBA-15 system. Hence, the Zn<sup>2+</sup> cation causes significant network modification and a concomitant increase in the non-bridging O bond (Si=O···Zn) formation. The corresponding <sup>1</sup>H MAS data (see Figure 11b, Table S1) exhibits large changes to the nature of the H network on the SBA-15 surface. While the native SBA-15 system exhibits well resolved –OH resonances in the range δ 0.6 - 1.6 ppm (isolated surface silanol Si–OH species with no nearby <sup>1</sup>H species to promote H-bonding), at δ 3.5 ppm (isolated surface silanol Si–OH species with H-bonding/proximity to small residual non-bridging O components), and physisorbed H<sub>2</sub>O represented by resonances in the range δ 5.0 - 6.0 ppm, the <sup>1</sup>H MAS NMR data from Zn/SBA-15 system suggests a more strongly H-bonded system characterised by much broader resonances. In this latter case, Zn incorporation has markedly increased the population of network modified non-bridging Si=O···Zn species, thus driving the majority of the –OH species into a H-bonded network with non-bridging O species as evidenced by the broad dominant <sup>1</sup>H resonance at δ ~3.7 ppm. Furthermore, the wettability of the Zn modified Zn/SBA-15 surface has increased as evidenced by the greater intensity of the H<sub>2</sub>O resonance at δ ~6.0 ppm suggesting a higher affinity for physisorbed H<sub>2</sub>O. In this case, the broader <sup>1</sup>H linewidth and more downfield <sup>1</sup>H chemical shift of the H<sub>2</sub>O resonance indicates increased H-bonding within clusters of surface H<sub>2</sub>O molecules with less mobility<sup>51</sup>. The large increase in the Q<sup>3</sup> Si species, together with the loss of the majority of the surface silanol (Si–OH) species and the increase of OH which are H-bonded to network modified structures (such as non-bridging O) suggests that the Zn incorporation is not confined strictly to the SBA-15 surface, but creates a substitution of Si into the bulk structure.

In contrast, the incorporation of Pt towards the formation of the analogous Pt/SBA-15 system induces very different response from the SBA-15 surface and bulk speciation. The  $^{29}\text{Si}$  MAS NMR data of Figure 11a suggests that the introduction of Pt also causes more modest network modification as evidenced by the increased intensity  $Q^3$  resonances by  $\sim 10\%$  and a reduction of NC from to 3.65 (see Table 4). Although there is some evidence of H-bonded  $-\text{OH}$  species to non-bridging O species through network modification from the broader  $\delta \sim 3.8$  ppm resonance in the  $^1\text{H}$  MAS NMR data, this contribution is very much reduced in comparison to that observed in the Zn/SBA-15 system, with most of the surface H speciation remaining unperturbed from that characterising the native SBA-15. This suggests that most of the network modification induced by Pt incorporation is confined to the surface, and that the majority of  $Q^3$  involve Si-O-Pt linkages which tether Pt nanoparticle formation to the SBA-15 surface, or non-bridging O structures to form these linkages.

The  $^{29}\text{Si}$  MAS NMR data for the Pt-Zn/SBA-15 series (see Figure 11a and Table 4) exhibits the largest amount of network modification with (on average)  $\sim 33\%$  of the observed Si speciation now assuming a  $Q^3$  identity.

From the NMR data, it is therefore evident that  $\text{Zn}^{2+}$  has a stronger affinity to substitute the  $\text{Si}^{4+}$  than  $\text{Pt}^{2+}$ , the effect of which can go beyond the top surface to the interior of the SBA-15 wall structure. It is interesting to note that the higher Zn content samples such as Zn/SBA-15 and  $\text{Pt}_5\text{Zn}_5/\text{SBA-15}$  display a broad resonance at a chemical shift value of 3.4-3.6 ppm and 5.0-6.0 ppm of water clusters, indicative that the Zn modified surfaces have a higher affinity for water (high mobility of hydroxyl units for chemical exchange) (Fig. S7b) than that of hydrophobic Pt modified surfaces with hydroxyl units of less mobility. The  $\text{Pt}_2\text{Zn}_8/\text{SBA-15}$  is anticipated to display similar affinity for water although this sample had been extensively dried before the measurement.

The  $^{195}\text{Pt}$  static NMR data from the  $\text{Pt}_8\text{Zn}_2/\text{SBA-15}$  system presented in Figure 10c corroborates the SAXS, TEM and APT findings (reported above) that Pt nanoparticles and  $\text{PtO}_2$  are present in this sample. Even though the concentration of the  $^{195}\text{Pt}$  nucleus on the SBA-15 surface is low, the frequency sweep experiment using the ATMA probe and the VOCS spectral accumulation method (50 kHz acquisition intervals) is sensitive enough to detect these Pt species. From a direct comparison with 5 nm Pt nanoparticles supported on carbon black and with well-ordered  $\text{PtO}_2$  as shown in Figure 11c, enough spectral features are discernible to clearly identify these Pt metal and Pt oxide components. A previous  $^{195}\text{Pt}$  NMR study of Pt metal nanoparticles has demonstrated that the very broad  $^{195}\text{Pt}$  static lineshape ( $\sim 3.2$  MHz linewidth) can be analysed by the core-shell model, and estimates of the nanoparticle size can be attempted.<sup>52</sup> The lack of a narrow and discernible feature at a Knight shift of  $-35350$  ppm representing bulk Pt metal, and with intensity still present from the core-shell Knight shifts in the range of  $-30000$  -  $-35000$  ppm, it can be estimated that the Pt nanoparticle sizes in  $\text{Pt}_8\text{Zn}_2/\text{SBA-15}$  are in the 2-5 nm range. These estimates of dimension are consistent with the nanoparticle dimensions derived by SAXS and TEM methods. From the intensities measured in this  $^{195}\text{Pt}$  static

NMR data it can be observed that comparable amounts of diamagnetic  $\text{PtO}_2$  accompany the Pt nanoparticle formation. This is likely to form on the exterior of the Pt nanoparticles that form in the 2-5 nm range; the Zn that decorates the Pt nanoparticles and the  $\text{PtO}_2$  that coats these entities will effectively increase the intrinsic size of the deposited nanoparticles.

**Table 4.**  $^{29}\text{Si}$  MAS NMR data and network connectivity values

| Sample                          | $Q^2$                          |                 | $Q^3$                          |                 | $Q^4$                          |                 | NC   |
|---------------------------------|--------------------------------|-----------------|--------------------------------|-----------------|--------------------------------|-----------------|------|
|                                 | $\delta_{\text{iso}}$<br>(ppm) | I(%)<br>$\pm 3$ | $\delta_{\text{iso}}$<br>(ppm) | I(%)<br>$\pm 3$ | $\delta_{\text{iso}}$<br>(ppm) | I(%)<br>$\pm 3$ |      |
| SBA-15                          | -91.1                          | 4               | -102.5                         | 12              | -111.2                         | 84              | 3.81 |
| Zn/<br>SBA-15                   | -89.6                          | 4               | -101.6                         | 30              | -110.8                         | 66              | 3.62 |
| Pt/<br>SBA-15                   | -92.3                          | 7               | -101.8                         | 22              | -110.2                         | 71              | 3.65 |
| $\text{Pt}_8\text{Zn}_2/SBA-15$ | -91.6                          | 4               | -101.9                         | 33              | -110.4                         | 63              | 3.60 |
| $\text{Pt}_5\text{Zn}_5/SBA-15$ | -91.2                          | 6               | -101.6                         | 34              | -110.1                         | 60              | 3.54 |
| $\text{Pt}_2\text{Zn}_8/SBA-15$ | -92.3                          | 5               | -101.0                         | 32              | -110.4                         | 63              | 3.58 |

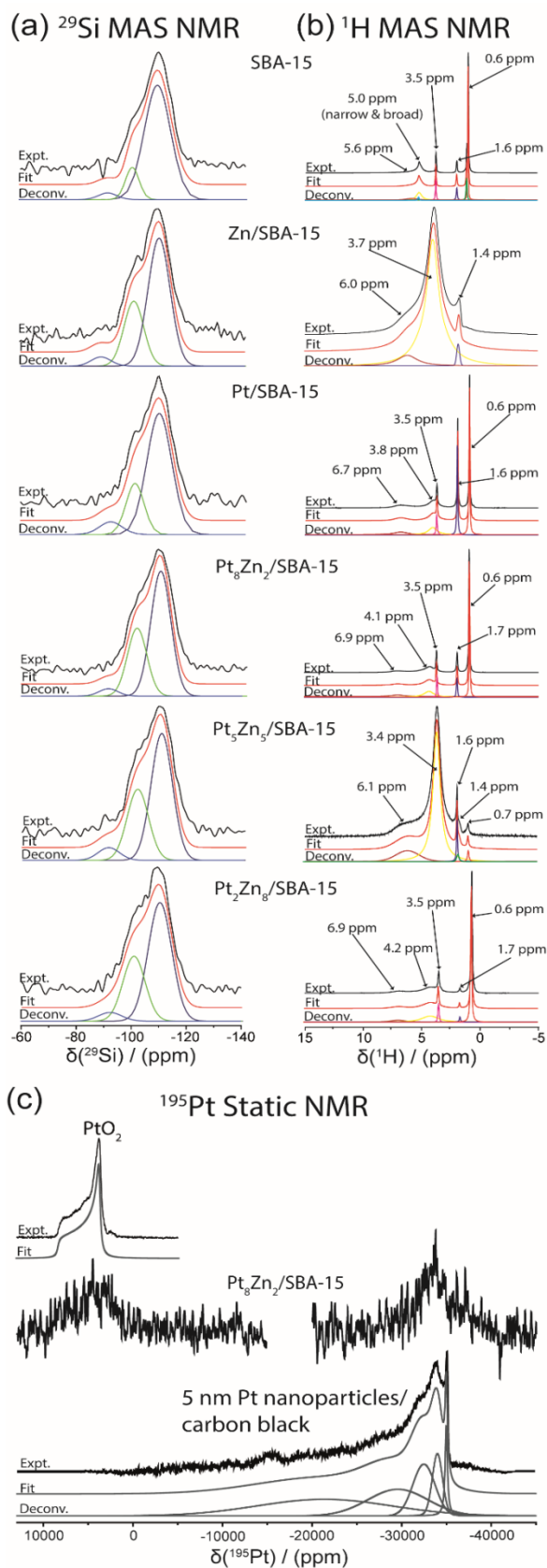


Figure 11.  $^{29}\text{Si}$ ,  $^1\text{H}$  and  $^{195}\text{Pt}$  NMR deconvoluted and simulated spectra

Atom Probe Tomography was performed on typical  $\text{Pt}_2\text{Zn}_8/\text{SBA-15}$  sample to identify the spatial distributions of the zinc compared to the platinum particles. Figure 12 shows 3 end-on atom maps from the green cross sections and 1 side-view atom map from the blue cross section, with each cross section 1 nm thick. The end-on maps indeed show that the Zn ions (yellow) are widely dispersed across the silica, and the platinum atoms cluster together forming spherical nanoparticles in the channels. The end-on images show the platinum particle size of around 4 nm which correlates with the size distribution expected from the TEM and SAXS results. It appears the distribution of zinc ions around the platinum particles is random, with some zinc ions adjacent to the platinum and others in regions without any platinum. This also indicates that the interaction of the zinc with the silica walls is much stronger than the interaction with the platinum. There are very small areas of zinc which are slightly more aggregated, and these could be rare clusters in the material. As there is no Zn crystallinity seen in the WAXS data and no long-range zinc interaction in the XAS indicating that these regions are rare and very small.

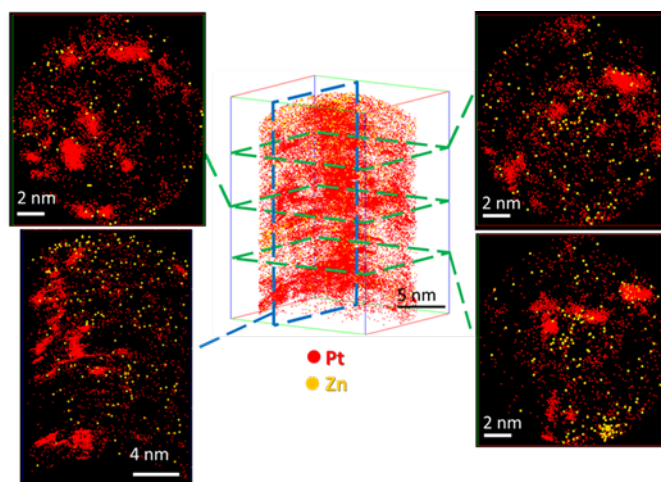


Figure 12. APT cross sections showing platinum (red) and zinc (yellow) species. Green cross sections show end-on images, looking down the SBA-15 channels and blue cross section shows the side-view image. Each cross section is 1 nm in thickness.

#### Discussion

The above characterization clearly indicates that small platinum containing nanoparticles can be formed in SBA-15 channels without using surfactants or polymers by the described porous template method. The platinum precursors after reduction give primarily encapsulated metallic Pt nanoparticles with a narrow size distribution, smaller than the pore size inside the porous channels either by wet impregnation using purely Pt precursor or mixed Pt and Zn precursors (no blockage to the larger internal pores). Thus, this method appears to be suitable to prepare highly dispersed supported nanoparticles as catalysts. As stated, it is surprising to detect the absence of Zn containing nanoparticles for the same preparation over pure Zn precursors. Instead, the zinc forms homogeneously dispersed, but isolated, oxidic Zn-O tetrahedra within the internal

silica walls where no equivalent Pt species are anchored. This demonstrates the internal walls of the porous template can exert a significant influence on structure and morphology of nanoparticles growth therein. The reason for the propensity for zinc to anchor on the silica walls, compared to platinum, is not yet known, but this may be related to similar tetrahedral structure of silica for epitaxy-like anchoring of Zn species. In addition, zinc is more oxophilic than platinum<sup>53</sup> which could lead to greater interaction and affinity between the internal silica surface than with the platinum, meaning that zinc preferentially disperses or wets to this support while platinum forms particles within the channels. This point is also demonstrated by the <sup>1</sup>H NMR studies which showed the high affinity for water molecules to lead to water clustering in the case of surfaces heavily modified with Zn species than that of Pt rich surfaces. Also, there are reciprocal modifications of the confined lattices for both encapsulated core-shell particles and host due to their structural and electronic interactions. In contrast to the model of AgNi system in SBA-15 showing a clearly thermodynamic more stable Ni@Ag core shell particles of tunable dimensions (light element in core and heavy element in shell)<sup>54</sup> which is adopted also by many other transition metal/metal oxide systems of CuO-Au and CuO-Ag,<sup>55,56</sup> it is clearly not replicated in this system. It is noted that the immobilization of oxidic Zn-O tetrahedral species on internal silica surface is somehow akin to the modified zeolite frameworks which may result from anchoring of two or three surface oxygens with terminal OH formed from Zn precursors dependent on surface acidity and impurities during their catalyst synthesis. The difference in spacing between O terminations over the internal amorphous silica surface and that of zinc oxide or hydroxide, can apparently avoid the extensive deposition of these phases on the wall, which maintains the oxidic Zn-O tetrahedral species in isolation. It is shown from this study that such atomically dispersed zinc sources from surrounding internal walls can be used to decorate the formed Pt nanoparticle in close proximity after reduction. Temperature programmed reduction (TPR) shown in the supporting information (S6) indicates that a significant co-reduction of Zn atoms from the modified silica walls is observed. This is shown from the enhanced Pt reduction peak indicating the partial reduction of the single Zn atoms to decorate the Pt nanoparticles<sup>57</sup>. Conventionally, decoration of supported precious metal nanoparticles with transition metal atoms is commonly achieved by exposing the metal nanoparticles on low surface area transition metal oxide supports, such as Cu/ZnO<sup>31</sup> or Pd/ZnO<sup>58</sup>, to hydrogen gas with the formation of uncontrolled CuZn or PdZn content at the interface, through hydrogen spillover at elevated temperature. It is believed this new observation on the strong wall effects may lead to a development of new encapsulated single atom decorated metal catalysts dispersed in porous templates.

#### Conclusions

Although SBA-15 has been shown to promote the typical core-shell growth in bimetallic compounds such as AgNi under mild reduction, this does not translate into the PtZn system. The PtZn/SBA-15 catalysts show clearly segregated metallic behavior, with isolated Zn tetrahedra on the silica channel walls, and small Pt monometallic

particles in the channels. The isolated [ZnO<sub>4</sub>]<sup>6-</sup> tetrahedra have no extended structure or crystallinity and do not appear in the microscopic images. The Pt particles on the other hand, are majority metallic, with a platinum oxide surface layer and are totally incorporated inside the channels of the SBA-15, not appearing on the surface of the support. The filling of the SBA-15 channels with ZnPt particles also leads to the alteration of the SBA-15 lattice structure. The use of SBA-15 as a support for formation of bimetallic nanoparticles is not trivial across various elemental compositions. In correlation with the previously reported core-shell synthesis we can see for the first time that the internal silica walls have a significant influence on the structure of the Pt particles formed inside. Zinc appears to form isolated sites across the silica while Pt is less attracted to the walls and forms the encapsulated particles in the channels. The interaction of isolated single atomic site zinc adjacent to platinum after reduction could lead to development of a new synthesis method for atomic decorated metal nanoparticles.

## Experimental

### Materials and Methods

Platinum nitrate solution was sourced from Alfa Aesar. Zinc nitrate and mesoporous silica SBA-15 were bought from Sigma Aldrich along with ethanol (99%) solvent.

### Synthetic Procedures

PtZn(SBA-15) nanoparticles were synthesized without the use of surfactants using an incipient wetness technique. 2 mL pre-prepared platinum nitrate, zinc nitrate and ethanol solution was ground into 500 mg SBA-15 using a pestle and mortar. After 10 minutes of grinding the powder was left to fully dry in air for at least 3 hours. The fully dried powder was calcined at 400 °C with a ramp rate of 2 °C/min under nitrogen and then reduced at the same temperature under 5 % hydrogen in argon for 4 hours. The sample was cooled to room temperature and ground for testing.

### Transmission Electron Microscopy

Homogeneity of the metal dispersion inside the SBA-15 channels was examined by TEM using a JEOL 3000F transmission electron microscope operated at 300 kV. TEM specimens were prepared by dispersing the dry catalyst powder in ethanol using sonication then pipetting 5 µl of the sample dispersion onto holey-carbon coated copper grids. Secondary electron imaging and EDX mapping was performed to ensure the particles were inside the channels and to investigate the particle compositions. The samples were ground between two glass slides and dusted onto a holey carbon coated Cu TEM grid. The samples were examined in the JEM 2800 Transmission Electron Microscope using the following instrumental conditions: Voltage (kV) 200; C2 aperture (µm) 30 and 50; Dark-field (Z-contrast) imaging in scanning mode using an off-axis annular detector. Compositional analysis by X-ray emission detection in the scanning mode.

### Low Energy Ion Scattering

High sensitivity-low energy ion scattering (HS-LEIS) was used to probe the change in composition with particle depth. The experiments were performed in a combined elevated-pressure reaction cell-ultrahigh vacuum (UHV) system. Sample preparation and characterization were conducted in the primary UHV chamber (base pressure,  $2 \times 10^{-9}$  Torr). HS-LEIS were measured by IONTOF Qtac100 using  $20\text{Ne}^+$  (5 keV) as ion source. The scattering angle was  $145^\circ$ .

#### X-ray Absorption Spectroscopy

X-ray Absorption Spectroscopy, used to investigate the local structure and properties of the catalyst components, was undertaken at Diamond Light Source, beamline B18. Both the Pt L3- and Zn K-edges were measured where appropriate for each sample. The XAS measurements were conducted in the transmission geometry, in a step scan mode, using a silicon 311 double crystal monochromator. Typically, 150mg of sample was ground and pressed into a 13mm diameter pellet. The Pt L3-edge was measured between 11336 and 12364 eV and the Zn K-edge was measured between 9462 and 10512 eV.

#### Wide and Small Angle X-ray Scattering

WAXS was collected at beamline I22 of the Diamond Light Source. Data collection was performed at 18keV using the Pilatus3-2M-DLS-L detector with a refined sample detector distance of 177 mm calibrated using a NIST 640c silicon standard reference material. Scans were performed ex-situ within 2 mm polycarbonate capillaries with total data acquisition time per sample of 1 s. The collected 2D images were corrected for incident flux, transmission, and collection time, and reduced to 1D patterns using the DAWN software package<sup>59,60</sup>. An empty capillary was used to subtract the background from the data. A bare SBA-15 sample was also collected for comparative purposes. Data was processed with base-line subtraction to allow for direct comparison and peak fitting.

SAXS was collected at beamline I22 of the Diamond Light Source. Data collection was performed at 18keV using a Pilatus3-2M detector with a refined sample detector distance of 9.8 m, calibrated using a silicon nitride grating with a 100nm period. Scans were performed ex-situ within 2 mm polycarbonate capillaries with total data acquisition time per sample of 1 s. The collected 2D images were corrected for incident flux, transmission, and collection time, and reduced to 1D patterns using the DAWN software package. An empty capillary was used to subtract the background from the data. A bare SBA-15 sample was also collected for comparative purposes. Peak fitting was conducted on the (200) reflection to extract the related lattice parameters of the SBA-15.

#### Solid State $^{29}\text{Si}$ , $^1\text{H}$ and $^{195}\text{Pt}$ NMR

Single pulse  $^{29}\text{Si}$  MAS NMR measurements were performed at 7.05 T using a Varian/Chemagnetics InfinityPlus spectrometer operating at a  $^1\text{H}$  and  $^{29}\text{Si}$  Larmor frequencies ( $\nu_0$ ) of 59.6 and 300.1 MHz, respectively. These experiments were performed using a Bruker 7 mm HX probe which enabled a

MAS frequency of 5 kHz to be implemented. Pulse length calibration was performed on solid kaolinite from which a  $\pi/2$  pulse time of  $4.5 \mu\text{s}$  was measured. Quantitative measurements were achieved with a  $\pi/3$  pulse of  $3.0 \mu\text{s}$  angle, together with a recycle delay of 240 s. To aid the simulation and deconvolution through accurate identification of the speciation in the MAS NMR data, analogous  $^1\text{H}$ - $^{29}\text{Si}$  cross-polarisation MAS (CPMAS) measurements were undertaken using an initial  $^1\text{H}$   $\pi/2$  pulse of  $4 \mu\text{s}$ , a contact time of 4 ms, a CP ramp ranging from 75% and 100%, and a recycle delay of 5 s were utilised. These data are shown in the Supporting Information (Fig. S7a). For both the single pulse MAS and CPMAS experiments heteronuclear  $^1\text{H}$  decoupling was implemented during data acquisition. All  $^{29}\text{Si}$  chemical shifts are reported against the IUPAC recommended primary  $^{29}\text{Si}$  reference of  $\text{Me}_4\text{Si}$  ( $\delta_{\text{iso}}$  0.0 ppm) via a solid kaolinite secondary reference at  $\delta_{\text{iso}}$  -92 ppm.<sup>44</sup>

Single pulse  $^1\text{H}$  MAS measurements were performed at 9.4 T using a Bruker Avance HD spectrometer, operating at a  $^1\text{H}$   $\nu_0$  of 398.8 MHz and a MAS frequency of 12 kHz. These experiments were performed using a Bruker 4 mm HX probe which enabled a MAS frequency of 12 kHz to be achieved. A  $^1\text{H}$   $\pi/2$  pulse time of  $2.50 \mu\text{s}$  was calibrated on solid  $\alpha$ -alanine, with a  $\pi/4$  pulse of  $1.25 \mu\text{s}$  being implemented together with a recycle delay was 5 s. All  $^1\text{H}$  chemical shifts are reported against the IUPAC recommended primary  $^1\text{H}$  reference of  $\text{Me}_4\text{Si}$  ( $\delta_{\text{iso}}$  0.0 ppm) via a solid  $\alpha$ -alanine secondary reference ( $\text{CH}_3$  resonance) at  $\delta_{\text{iso}}$  1.1 ppm.<sup>44</sup>

All  $^{195}\text{Pt}$  static solid state NMR measurements were conducted on a Bruker Avance HD 7.05 T spectrometer ( $\nu_0 = 64.5$  MHz) using a novel Bruker 7 mm static solids auto-tuning (ATMA) probe. The ATMA probe allows consistent automated tuning across the  $^{195}\text{Pt}$  Knight/chemical shift range spanning 3.6 MHz, giving highly reproducible Variable Offset Cumulative Spectroscopy (VOCS)<sup>45,46,52</sup> data which are comparable to our previously reported Field Sweep Fourier Transform (FSFT) method<sup>52</sup>. The VOCS method with automatic probe tuning stepped through the  $^{195}\text{Pt}$  spectral range at 50 kHz frequency intervals and applied a Hahn echo ( $\pi/2 - \pi$  - acquire) experiment which employed  $4 / 8 \mu\text{s}$   $\pi/2 / \pi$  pulse durations for data acquisition at each frequency step. A total of 250,000 transients were acquired per slice with a recycle delay of 0.1 s used for the fast relaxing Pt metal (Knight shifted) region, whereas the more diamagnetic  $\text{PtO}_2$  region used a longer recycle delay of 7 s with only 5000 transients being acquired at this higher frequency (downfield) region. Pulse time calibration and the  $^{195}\text{Pt}$  shift referencing was performed on a Pt metal sample which served as secondary reference ( $\delta_{\text{iso}}$  -35,350 ppm) against the primary IUPAC reference of 1.2 M  $\text{Na}_2\text{PtCl}_6(\text{aq})$  ( $\delta_{\text{iso}}$  0.0 ppm).<sup>52</sup>

#### Atom Probe Tomography

The APT specimens were prepared by the following procedure. A drop of SBA particle dispersion was placed onto a Si flat wafer, which was covered by a 200-nm thick protective Cr layer<sup>61</sup>. Needle-shaped APT specimens were prepared from the Si flat sample by a site-specific

lift-out procedure using a FEI Helios G4 CX focused ion beam (FIB)/scanning electron microscope. The APT experiments were conducted in a CAMECA LEAP 5000 XR instrument equipped with an ultraviolet laser with a spot size of 2  $\mu\text{m}$  and a wavelength of 355 nm. The detection efficiency of this state-of-the-art microscope is ~52%. Data was acquired in laser pulsing mode at a specimen temperature of 60 K, with a target evaporation rate of 3 ions per 1000 pulses, a pulsing rate of 125 kHz, laser pulse energy of 70 pJ. The APT data were reconstructed and analysed using the commercial IVAS 3.6.14™ software.

#### ASSOCIATED CONTENT

**Supporting Information.** Supporting figures including TEM and EDX maps of series of catalysts, EXAFS, TPR and NMR. This material is available free of charge via the Internet at <http://pubs.acs.org>.

#### AUTHOR INFORMATION

##### Corresponding Author

\*edman.tsang@chem.ox.ac.uk

##### Author Contributions

The manuscript was written through contributions of all authors. / All authors have given approval to the final version of the manuscript. / ‡These authors contributed equally.

##### Funding Sources

The financial support of EPSRC and Johnson Matthey are acknowledged.

#### ACKNOWLEDGMENT

The financial support of EPSRC and Johnson Matthey (JM) are acknowledged. The authors would also like to thank staff from Diamond Light Source, UK (B18 and I11) for access to beamtime under proposal numbers SP16316 and SM16583, Gregory Goodlet and Don Ozkaya for TEM/EDX images and Xiamen University for LEIS. JVH thanks the EPSRC, the University of Warwick and the Birmingham Science City Program for partial funding of the solid state NMR infrastructure at Warwick. The latter program accessed the Birmingham Science City Advanced Materials Project 1: Creating and Characterising Next Generation Advanced Materials, which derived support from Advantage West Midlands (AWM) and the European Regional Development Fund (ERDF).

#### REFERENCES

1. Gerland P, Raftery AE, Ševčíková H, *et al.* World population stabilization unlikely this century. *Science* 2014,**346**(6206),234–7.
2. Shafiee S, Topal E. When will fossil fuel reserves be diminished? *Energy Policy* 2009,**37**(1),181–9.
3. Hodgson P. Nuclear power and the energy crisis. *Mod Age* 2008,**50**(3),238.
4. Alayoglu S, Nilekar AU, Mavrikakis M, Eichhorn B. Ru-Pt core-shell nanoparticles for preferential oxidation of carbon monoxide in hydrogen. *Nat Mater* 2008,**7**(4),333–8.
5. Zhang S, Metin Ö, Su D, Sun S. Monodisperse AgPd alloy nanoparticles and their superior catalysis for the dehydrogenation of formic acid. *Angew Chemie - Int Ed* 2013,**52**(13),3681–4.
6. Balakrishnan N, Joseph B, Bhethanabotla VR. Effect of platinum promoters on the removal of O from the surface of cobalt catalysts: A DFT study. *Surf Sci* 2012,**606**(5–6),634–43.
7. Cybulskis VJ, Bukowski BC, Tseng HT, *et al.* Zinc Promotion of Platinum for Catalytic Light Alkane Dehydrogenation: Insights into Geometric and Electronic Effects. *ACS Catal* 2017,**7**(6),4173–81.
8. Yarulin A, Berguerand C, Yuranov I, C??rdenas-Lizana F, Prokopyeva I, Kiwi-Minsker L. Pt-Zn nanoparticles supported on porous polymeric matrix for selective 3-nitrostyrene hydrogenation. *J Catal* 2015,**321**,7–12.
9. Liu G, Zeng L, Zhao ZJ, Tian H, Wu T, Gong J. Platinum-Modified ZnO/Al<sub>2</sub>O<sub>3</sub> for Propane Dehydrogenation: Minimized Platinum Usage and Improved Catalytic Stability. *ACS Catal* 2016,**6**(4),2158–62.
10. Lopez-Sanchez JA, Dimitratos N, Hammond C, *et al.* Facile removal of stabilizer-ligands from supported gold nanoparticles. *Nat Chem* 2011,**3**(7),551–6.
11. Mishra PK, Saxena A, Rawat AS, Dixit PK, Kumar R, Rai PK. Surfactant-Free One-Pot Synthesis of Low-Density Cerium Oxide Nanoparticles for Adsorptive Removal of Arsenic Species. *Environ Prog Sustain Energy* 2017,**37**(1).
12. Pritchard J, Morris L, Walsh D, *et al.* Synthesis of Well-Defined, Surfactant-Free Co<sub>3</sub>O<sub>4</sub> Nanoparticles: The Impact of Size and Manganese Promotion on Co<sub>3</sub>O<sub>4</sub> Reduction and Water Oxidation Activity. *Catal Letters* 2017,**0**(0),0.

13. Tao L, Zhao Y, Zhao Y, *et al.* A surfactant free preparation of ultradispersed surface-clean Pt catalyst with highly stable electrocatalytic performance. *J Phys Chem Solids* 2018,**113**(July 2017),61–6.
14. Yin H, Tang H, Wang D, Gao Y, Tang Z. Facile synthesis of surfactant-free Au cluster/graphene hybrids for high-performance oxygen reduction reaction. *ACS Nano* 2012,**6**(9),8288–97.
15. Wang ZJ, Xie Y, Liu CJ. Synthesis and characterization of noble metal (Pd, Pt, Au, Ag) nanostructured materials confined in the channels of mesoporous SBA-15. *J Phys Chem C* 2008,**112**(50),19818–24.
16. Kónya Z, Puentes VF, Kiricsi I, *et al.* Synthetic insertion of gold nanoparticles into mesoporous silica. *Chem Mater* 2003,**15**(6),1242–8.
17. Qiao B, Wang A, Yang X, *et al.* Single-atom catalysis of CO oxidation using Pt1/FeOx. *Nat Chem* 2011,**3**(8),634–41.
18. Flytzani-Stephanopoulos M, Gates BC. Atomically Dispersed Supported Metal Catalysts. *Annu Rev Chem Biomol Eng* 2012,**3**(1),545–74.
19. Thomas JM, Saghi Z, Gai PL. Can a single atom serve as the active site in some heterogeneous catalysts? *Top Catal* 2011,**54**(10–12),588–94.
20. Heiz U, Sanchez A, Abbet S, Schneider WD. Catalytic oxidation of carbon monoxide on monodispersed platinum clusters: Each atom counts. *J Am Chem Soc* 1999,**121**(13),3214–7.
21. Turner M, Golovko VB, Vaughan OPH, *et al.* Selective oxidation with dioxygen by gold nanoparticle catalysts derived from 55-atom clusters. *Nature* 2008,**454**(7207),981–3.
22. Kaden WE, Wu T, Kunkel WA, Anderson SL. Electronic structure controls reactivity of size-selected Pd clusters adsorbed on TiO<sub>2</sub> surfaces. *Science* 2009,**326**(5954),826–9.
23. Nakamura, I., Nakano, H., Fujitani, T., Uchijima, T., Nakamura J. Evidence for a special formate species adsorbed on the Cu–Zn active site for methanol synthesis. *Surf Sci* 1998,**402–404**,92–5.
24. J. Penzien, A. Abraham, J. A. van Bokhoven, A. Jentys, T. E. Müller, C. Sievers JAL. Generation and Characterization of Well-Defined Zn<sup>2+</sup>+Lewis Acid Sites in Ion Exchanged Zeolite BEA. *J Phys Chem B* 2004,**108**,4116–26.
25. Kozawa A. Ion-Exchange Adsorption of Zinc and Copper Ions on Silica. *Nucl Chem* 1961,**21**(324),315–24.
26. Connell G, Dumesic JA. The generation of Bronsted and Lewis acid sites on the surface of silica by addition of dopant cations. *J Catal* 1987,**105**(2),285–98.
27. Takewaki T, Beck LW, Davis ME. Zincosilicate CIT-6: A Precursor to a Family of BEA-Type Molecular Sieves. *J Phys Chem B* 1999,**103**(Copyright (C) 2012 American Chemical Society (ACS). All Rights Reserved.),2674–9.
28. Schweitzer NM, Hu B, Das U, *et al.* Propylene hydrogenation and propane dehydrogenation by a single-site Zn<sup>2+</sup> on silica catalyst. *ACS Catal* 2014,**4**(4),1091–8.
29. Kolyagin YG, Ivanova II, Ordonsky V V, Gedeon A, Pirogov YA. Methane Activation over Zn-Modified MFI Zeolite : NMR Evidence for Zn - Methyl Surface Species Formation. *J Phys Chem C* 2008,**112**,20065–9.
30. Orazov M, Davis ME. Catalysis by framework zinc in silica-based molecular sieves. *Chem Sci* 2016,**7**,2264–74.
31. Li MM-J, Zheng J, Qu J, *et al.* The remarkable activity and stability of a highly dispersive beta-brass Cu-Zn catalyst for the production of ethylene glycol. *Sci Rep* 2016,**6**(November 2015),20527.
32. Kang Y, Pyo JB, Ye X, Gordon TR, Murray CB. Synthesis, shape control, and methanol electro-oxidation properties of Pt-Zn alloy and Pt 3Zn intermetallic nanocrystals. *ACS Nano* 2012,**6**(6),5642–7.

33. Ammari F, Lamotte J, Touroude R. An emergent catalytic material: Pt/ZnO catalyst for selective hydrogenation of crotonaldehyde. *J Catal* 2004,**221**(1),32–42.
34. Yu C, Xu H, Ge Q, Li W. Properties of the metallic phase of zinc-doped platinum catalysts for propane dehydrogenation. *J Mol Catal A Chem* 2007,**266**(1–2),80–7.
35. Guda SA, Guda AA, Soldatov MA, *et al.* Optimized Finite Difference Method for the Full-Potential XANES Simulations: Application to Molecular Adsorption Geometries in MOFs and Metal-Ligand Intersystem Crossing Transients. *J Chem Theory Comput* 2015,**11**(9),4512–21.
36. Bunău O, Joly Y. Self-consistent aspects of x-ray absorption calculations. *J Phys Condens Matter* 2009,**21**(34),345501.
37. Mei B, Becerikli A, Pougin A, *et al.* Tuning the acid/base and structural properties of titanate-loaded mesoporous silica by grafting of zinc oxide. *J Phys Chem C* 2012,**116**(27),14318–27.
38. Mansour AN, Cook JW, Sayers DE. Quantitative technique for the determination of the number of unoccupied d-electron states in a platinum catalyst using the L<sub>2,3</sub> x-ray absorption edge spectra. *J Phys Chem* 1984,**88**(11),2330–4.
39. Ichikuni N, Iwasawa Y. In situ d electron density of Pt particles on supports by XANES. *Catal Letters* 1993,**20**(1–2),87–95.
40. Short DR, Mansour AN, Cook JW, Sayers DE, Katzer JR. X-Ray absorption edge and extended x-ray absorption fine structure studies of PtTiO<sub>2</sub> catalysts. *J Catal* 1983,**82**(2),299–312.
41. Lytle FW, Wei PSP, Gregor RB, Via GH, Sinfelt JH. Effect of chemical environment on magnitude of x-ray absorption resonance at LIIedges. *Studies on metallic elements, compounds, and catalysts. J Chem Phys* 1979,**70**(11),4849–55.
42. Bressler I, Pauw BR, Thünemann AF, IUCr. *McSAS*: software for the retrieval of model parameter distributions from scattering patterns. *J Appl Crystallogr* 2015,**48**(3),962–9.
43. Pauw BR, Pedersen JS, Tardif S, Takata M, Iversen BB, IUCr. Improvements and considerations for size distribution retrieval from small-angle scattering data by Monte Carlo methods. *J Appl Crystallogr* 2013,**46**(2),365–71.
44. Hung-Kai T, J. PS, Gowsihan P, *et al.* Phosphate content affects structure and bioactivity of sol-gel silicate bioactive glasses. *Int J Appl Glas Sci* 2017,**8**(4),372–82.
45. Greasley SL, Page SJ, Sirovica S, *et al.* Controlling particle size in the Stöber process and incorporation of calcium. *J Colloid Interface Sci* 2016,**469**,213–23.
46. Lin Z, Jones JR, Hanna J V, Smith ME. A multinuclear solid state NMR spectroscopic study of the structural evolution of disordered calcium silicate sol-gel biomaterials. *Phys Chem Chem Phys* 2015,**17**(4),2540–9.
47. Macon ALB, Page SJ, Chung JJ, *et al.* A structural and physical study of sol-gel methacrylate-silica hybrids: intermolecular spacing dictates the mechanical properties. *Phys Chem Chem Phys* 2015,**17**(43),29124–33.
48. Xiang Y, Du J, Skinner LB, *et al.* Structure and diffusion of ZnO-SrO-CaO-Na<sub>2</sub>O-SiO<sub>2</sub> bioactive glasses: A combined high energy X-ray diffraction and molecular dynamics simulations study. *RSC Adv* 2013,**3**(17),5966–78.
49. Rosenthal AB, Garofalini SH. Structural Role of Zinc Oxide in Silica and Soda-Silica Glasses. *J Am Ceram Soc* 2005,**70**(11),821–6.
50. McKeown DA, Muller IS, Buechele AC, Pegg IL. Local environment of Zn in zirconium borosilicate glasses determined by X-ray absorption spectroscopy. *J Non Cryst Solids* 2000,**261**(1),155–62.
51. Grünberg B, Emmler T, Gedat E, *et al.* Hydrogen bonding of water confined in mesoporous silica MCM-41 and SBA-15

- studied by  $^1\text{H}$  solid-state NMR. *Chem - A Eur J* 2004,**10**(22),5689–96.
52. Rees GJ, Orr ST, Barrett LO, *et al.* Characterisation of platinum-based fuel cell catalyst materials using  $^{195}\text{Pt}$  wide-line solid state NMR. *Phys Chem Chem Phys* 2013,**15**(40),17195–207.
  53. Kepp KP. A quantitative scale of oxophilicity and thiophilicity. *Inorg Chem* 2016,**55**(18),9461–70.
  54. Li MM-J, Ye L, Zheng J, *et al.* Surfactant-free nickel–silver core@shell nanoparticles in mesoporous SBA-15 for chemoselective hydrogenation of dimethyl oxalate. *Chem Commun* 2016,**52**(12),2569–72.
  55. Czaplinska J, Sobczak I, Ziolk M. Bimetallic AgCu/SBA-15 system: The effect of metal loading and treatment of catalyst on surface properties. *J Phys Chem C* 2014,**118**(24),12796–810.
  56. Liu X, Wang A, Li L, Zhang T, Mou CY, Lee JF. Structural changes of Au-Cu bimetallic catalysts in CO oxidation: In situ XRD, EPR, XANES, and FT-IR characterizations. *J Catal* 2011,**278**(2),288–96.
  57. Arroyo-Ramírez L, Chen C, Cargnello M, Murray CB, Fornasiero P, Gorte RJ. Supported platinum–zinc oxide core–shell nanoparticle catalysts for methanol steam reforming. *J Mater Chem A* 2014,**2**(45),19509–14.
  58. Liao F, Wu X-P, Zheng J, *et al.* Pd@Zn core–shell nanoparticles of controllable shell thickness for catalytic methanol production. *Catal Sci Technol* 2016,**6**(21),7698–702.
  59. Filik J, Ashton AW, Chang PCY, *et al.* Processing two-dimensional X-ray diffraction and small-angle scattering data in DAWN 2. *J Appl Crystallogr* 2017,**50**(3),959–66.
  60. Basham M, Filik J, Wharmby MT, *et al.* Data Analysis Workbench (DAWN). *J Synchrotron Radiat* 2015,**22**(3),853–8.
  61. Felfer P, Li T, Eder K, *et al.* New approaches to nanoparticle sample fabrication for atom probe tomography. *Ultramicroscopy* 2015,**159**,413–9.

Contents artwork

